RSC Advances

PAPER

Check for updates

Structural, magnetic and electronic properties of CrO$_2$ at multimegabar pressures

Shengxuan Huang, [iD]^a Xiang Wu,*^{b} Jingjing Niu^a and Shan Qin^a

As the only half-metallic ferromagnetic material in 3d transition metal dioxides, CrO$_2$ has attracted great scientific interest from materials science to physical chemistry. Here, an investigation into the structural, magnetic and electronic properties of CrO$_2$ under high pressure has been conducted by first-principles calculations based on density functional theory. Static calculations have predicted that CrO$_2$ undergoes structural transitions with the sequence of rutile-type → CaCl$_2$-type → pyrite-type → *Pnma* → (Fe$_2$P-type→) *I4/mmm* at high pressures. In addition, a transition from the ferromagnetic state to the non-magnetic state with the magnetic collapse of Cr is observed in CrO$_2$ at the pyrite–*Pnma* transition. This transition also delocalizes the 3d electrons of Cr and leads to a metallic character of CrO$_2$. The equation of state, elasticity and band gap for each energetically favorable phase of CrO$_2$ are determined. Our results not only bridge the gap about the high-pressure behavior of CrO$_2$ in previous studies but also extend our understanding of its properties up to multimegabar conditions. According to previous data and present results, we further discuss and summarize the high-pressure behavior of various AO$_2$ compounds. This can contribute to investigating properties of other AO$_2$ compounds or exploring novel materials at high pressures.

1. Introduction

The high-pressure behavior of AO$_2$ compounds, especially transition metal dioxides such as TiO$_2$, VO$_2$, CrO$_2$ and FeO$_2$, has attracted considerable interest in the field of materials science, condensed matter physics and geoscience.[1–10] For example, as a very important technological wide-gap semiconductor widely applied in photo-catalysts and electrochemical solar cells,[1,3] the band gap of TiO$_2$ can be modified by pressure, which extends its application in the industry.[11–13] The possibility to quench high-pressure forms of AO$_2$ compounds with different properties to ambient conditions is also potentially important to explore novel materials.[14] In addition, pressure-induced structural and electronic transitions of the simple compound VO$_2$ provide a good example to deeply understand and interpret the complicated Mott-like metal–insulator transition.[15,16] On the other hand, pressure-induced phase transitions of transition metal dioxides can serve as lower-pressure analogs to SiO$_2$, a critical component in the Earth's interior, especially when investigating ultrahigh-pressure polymorphs of SiO$_2$ in super-Earths' or extrasolar planets' interiors.[17–20]

In particular, CrO$_2$ attracts special interest since it is the only half-metallic (HM) ferromagnetic (FM) material in 3d transition metal dioxides. At ambient conditions, CrO$_2$ adopts the tetragonal rutile-type structure consisting of distorted edge-sharing CrO$_6$ octahedra similar to other transition metal dioxides [Fig. 1(a)]. Due to the crystal field of distorted CrO$_6$ octahedra, Cr t$_{2g}$ states are split into d$_{xy}$ with lower energy and d$_{yz}$–d$_{xz}$ with higher energy. The double-exchange interaction between the localized 3d electron occupying the d$_{xy}$ state and the delocalized 3d electron occupying half of the d$_{yz}$–d$_{xz}$ state near the Fermi level accounts for its HM and FM nature. The previous Andreev reflection experiment demonstrated that the spin polarization of the conduction electrons was more than 90%.[21] The saturation magnetization at 10 K was experimentally determined to be 1.92 μB per Cr.[22] Compared with other half-metals, the FM CrO$_2$ possesses a high Curie temperature of 390 K, which is also of technological importance to develop spintronic devices.[23] It is thus evident that these intriguing technological applications are associated with the structural, magnetic and electronic configurations of CrO$_2$. The properties are originated from the arrangement and interaction of electrons of CrO$_2$ within a typical structure.

High pressure, as one important thermodynamic parameter provides a unique way to decipher materials' structural, magnetic and electronic properties. The previous synchrotron X-ray diffraction (XRD) experiment and first-principle simulations both confirmed a second-order structural transition of CrO$_2$ from rutile-type to CaCl$_2$-type at ~12 GPa.[24–26] Theoretical computations predicted a further transition to the CaF$_2$-type structure at 89.6 GPa.[25] Recently, Wu *et al.*[27] predicted

^{a}Key Laboratory of Orogenic Belts and Crustal Evolution, MOE, School of Earth and Space Sciences, Peking University, Beijing 100871, P. R. China
^{b}State Key Laboratory of Geological Processes and Mineral Resources, China University of Geosciences, Wuhan, 430074, P. R. China. E-mail: wuxiang@cug.edu.cn
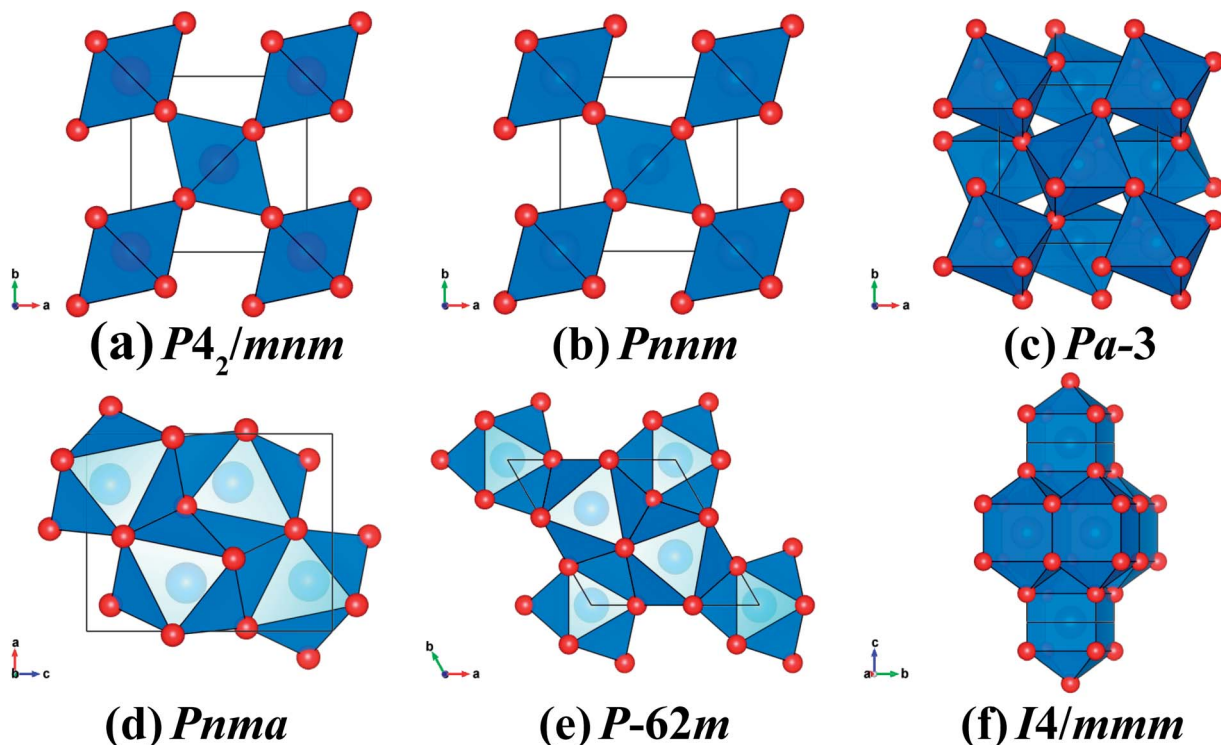
Fig. 1 The crystal structures of CrO$_2$ with (a) rutile-type, (b) CaCl$_2$-type, (c) pyrite-type, (d) *Pnma*, (e) Fe$_2$P-type and (f) *I4/mmm*. The blue and red spheres represent Cr and O atoms, respectively.

a pressure-induced phase transition sequence of rutile-type → CaCl$_2$-type → pyrite-type → CaF$_2$-type for CrO$_2$ whereas calculated results by the GGA method demonstrated that CrO$_2$ underwent a transition sequence of rutile-type → CaCl$_2$-type → PbO$_2$-type → pyrite-type at high pressures.[28] Obviously, there exists considerable discrepancy between different computational studies on CrO$_2$. It is worthwhile to note that heretofore the highest coordination number of Cr of various CrO$_2$ phases considered in previous investigations is eight whereas denser structures with higher coordination number are not included. In terms of magnetic properties of CrO$_2$ at high pressures, Kuznetsov *et al.*[29] predicted a magnetic transition from the FM state to the non-magnetic (NM) state accompanied by a half-metal to metal transition at ∼53 GPa. Whereas another theoretical study showed that the energetically favorable pyrite-type CrO$_2$ kept FM and HM up to ∼100 GPa.[28] In the meanwhile, Kim *et al.*[26] indicated that the phonon softening led to the FM–NM transition across a structural transition from the CaCl$_2$-type to a monoclinic structure at ∼61 GPa. Beyond ∼89 GPa, the CaF$_2$-type structure had the lowest enthalpy and correspondingly CrO$_2$ became a FM insulator. Therefore, the effect of pressure on the magnetic and electronic properties of CrO$_2$ still remains elusive and the physical properties of CrO$_2$ with much denser structures are poorly understood.

In this paper, we have performed first-principle calculations based on density functional theory (DFT) to fully investigate the structural, magnetic and electronic properties of CrO$_2$ at high pressures aiming to bridge the gap about the high-pressure behavior of CrO$_2$ between previous studies. Furthermore, we

extend the pressure range to investigate stable structures and properties of CrO$_2$ up to multimegabar conditions. Finally, comparing previous data with present results, we summarize the high-pressure behavior of various AO$_2$ compounds such as the phase transition sequence, elasticity and electronic properties.

2. Methods

High pressure can generally reduce bond distances and lead to the structural transition of one compound to form a denser structure. In addition, transition metal dioxides might undergo a similar phase transition sequence upon compression due to similar properties of transition metal elements. Thus, based on this empirical rule of the high-pressure crystal chemistry and extensive experimental and computational data, twelve candidate structures (rutile-type ($P4_2/mnm$), CaCl$_2$-type ($Pnnm$), PbO$_2$-type ($Pbcn$), pyrite-type ($Pa\bar{3}$), CaF$_2$-type ($Fm\bar{3}m$), $Pnma$, Fe$_2$P-type ($P\bar{6}2m$), CuAl$_2$-type ($I4/mcm$), $R\bar{3}m$, $I4/mmm$, AlB$_2$-type ($P6/mmm$), and Ni$_2$In-type ($P6_3/mmc$)) for CrO$_2$ were considered in the present study. First-principle calculations were performed based on DFT with the projected augmented wave method (PAW) implemented in Vienna ab-initio simulation package (VASP).[30–32] The Perdew–Burke–Ernzerhof (PBE) version of the generalized gradient approximations (GGA) was selected to treat the exchange correlation potential.[33] The kinetic energy cut-off was set to 1000 eV. The energy convergence criterion for the electronic self-consistent calculation was 10^{-6} eV. The total energy difference was converged to 1×10^{-5} eV per formula unit

Table 1 Calculated parameters of the third-order Birch–Murnaghan equation of state (energy per formula unit E_0, volume per formula unit V_0, bulk modulus K_0 and its pressure derivative K'_0 at zero pressure) of different CrO_2 phases. FM and NM represent ferromagnetic and non-magnetic, respectively. The previous experimental and theoretical data are extracted for comparison

Phase	E_0/f.u. (eV)	V_0/f.u. (Å³)	K_0 (GPa)	K'_0	Method and reference
FM-rutile	−25.231	29.13	228	4.7	This study
Rutile	—	28.50	235	5.0	Exp.[24]
Rutile	—	28.09	283	4.6	LDA[27]
FM-CaCl$_2$	−25.225	29.15	205	3.7	This study
CaCl$_2$	—	29.05	162	4.0	Exp.[24]
CaCl$_2$	—	28.32	179	4.3	LDA[27]
FM-PbO$_2$	−25.138	28.69	219	4.2	This study
NM-PbO$_2$	−24.785	27.57	213	4.7	This study
FM-pyrite	−24.727	26.85	249	4.4	This study
Pyrite	—	26.12	272	4.6	LDA[27]
NM-pyrite	−24.021	26.12	272	4.3	This study
FM-CaF$_2$	−24.401	26.35	254	4.4	This study
CaF$_2$	—	25.26	289	4.5	LDA[27]
NM-CaF$_2$	−23.523	25.60	276	4.3	This study
NM-Pnma	−23.434	24.95	254	4.0	This study
NM-Fe$_2$P	−22.844	23.98	286	4.1	This study
NM-CuAl$_2$	−22.533	24.79	262	4.3	This study
NM-R3m	−22.861	24.88	254	4.2	This study
NM-I4/mmm	−21.742	23.13	310	4.1	This study
NM-AlB$_2$	−18.704	24.97	241	4.1	This study
NM-Ni$_2$In	−21.203	24.28	240	4.3	This study

(f.u.) with respect to the energy cutoff or k-points. The force difference was converged to 1×10^{-3} eV Å^{-1} (less than 0.1 GPa). The spin-polarization of Cr without spin–orbit coupling in CrO_2 with various structures was included in the present study to obtain accurate physical information of CrO_2. The calculated sub-lattice magnetic moment per Cr in the rutile-type CrO_2 at 0 GPa was 2.04 μB in agreement with previous results and the HM property of the rutile-type CrO_2 could be accurately depicted.[22] The structural, elastic and magnetic properties of the rutile-type CrO_2 at 0 GPa could be reproduced by means of the GGA method. But Korotin et al.[34] suggested that the correlated effect of 3d electrons should be considered in CrO_2. Whether this system is strongly correlated is still an open question. On the one hand, comparing DFT results with low-temperature experimental data, Toropova et al.[35] concluded that the ordered phase of CrO_2 was weakly correlated. On the other hand, the calculated band gap of the rutile-type CrO_2 at 0 GPa was ~1.3 eV by the GGA method, much lower than the normal value ~2 eV.[34] Thus, in the present study, we used both the GGA and GGA + U methods to perform electronic density of state (DOS) calculations.[36] We applied $U = 3$ eV (the on-site Coulomb interaction parameter) and $J = 0.9$ eV (the Hund coupling constant) for Cr in GGA + U calculations as previous simulations did.[34,37]

For each crystalline phase, the atomic positions, unit-cell parameters and individual magnetic moments were allowed to relax at each given volume to obtain the minimum total energy. Energy-volume results were then fitted to the third-order Birch–Murnaghan equation of state (EoS) to obtain the corresponding parameters (volume per formula unit (V_0), bulk modulus (K_0), its pressure derivative (K'_0) and energy (E_0) at zero pressure).[38,39] In addition, the enthalpy ($H = E + PV$) of each

phase was compared with each other to identify the most stable structure at the given pressure. Furthermore, the DOS of various CrO_2 phases under selected pressure conditions were obtained by the static calculation, utilizing the tetrahedral smearing method with Blöchl corrections. The k-points grids were set as $12 \times 12 \times 20$ for rutile-type, $12 \times 12 \times 20$ for CaCl$_2$-type, $16 \times 16 \times 16$ for pyrite-type, $16 \times 24 \times 12$ for Pnma, $13 \times 13 \times 29$ for Fe$_2$P-type and $24 \times 24 \times 12$ for I4/mmm CrO_2 in DOS calculations. The phonon dispersion was calculated using the phonopy code by the supercell method.[40] $2 \times 3 \times 2$, $2 \times 2 \times 3$ and $3 \times 3 \times 2$ supercells were constructed for the Pnma, Fe$_2$P-type and I4/mmm CrO_2, respectively. The k-points grids in phonon calculations were set as $3 \times 5 \times 3$ for Pnma, $3 \times 3 \times 5$ for Fe$_2$P-type and $5 \times 5 \times 3$ for I4/mmm CrO_2, respectively.

3. Results and discussion

3.1. Structural stability and phase transitions

The corresponding EoS parameters of various candidate phases of CrO_2 are listed in Table 1. The present results of the FM rutile-type CrO_2 are consistent with previous high-pressure XRD data.[24] Calculated static enthalpy differences among various candidate phases of CrO_2 are plotted in Fig. 2 as a function of pressure up to 700 GPa based on aforementioned parameters. The present static calculations predict that CrO_2 will undergo five structural transitions upon compression with the sequence of rutile-type → CaCl$_2$-type → pyrite-type → Pnma → Fe$_2$P-type → I4/mmm. Calculated lattice constants and atomic coordinates of six phases at selected pressures are listed in Table 2.

The predicted rutile–CaCl$_2$ transition at 12 GPa is consistent with the experimental observation at 12 ± 3 GPa by high-pressure XRD and Raman spectroscopy.[24] The second
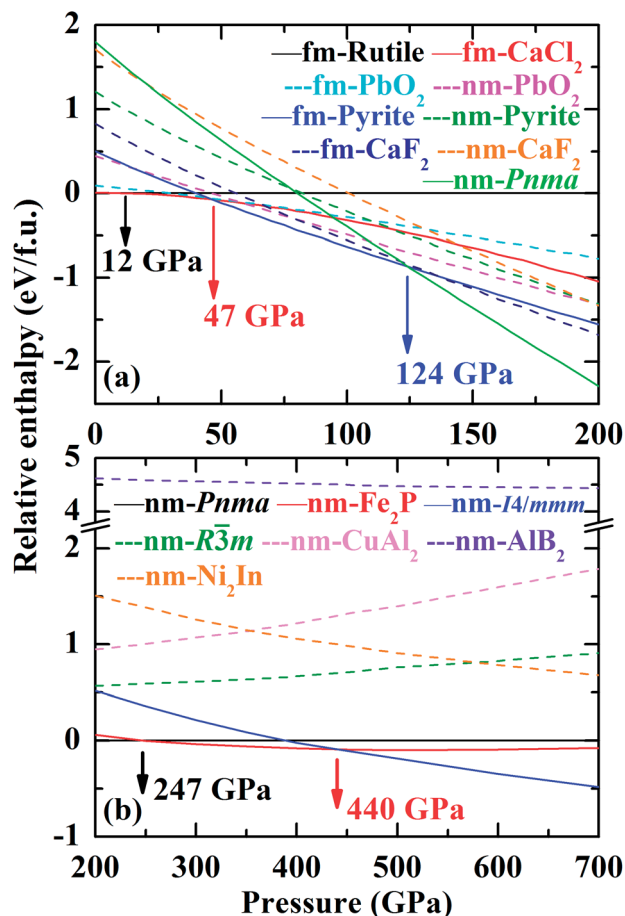
Fig. 2 Static enthalpy differences among various candidate phases of CrO₂ as a function of pressure. FM and NM represent ferromagnetic and non-magnetic, respectively. Structural transitions have been indicated by arrows.

the post-$Pnma$ phases for many AX_2 compounds.[17–19,41–43] It is to be noted that neither the AlB₂-type nor Ni₂In-type CrO₂ is an energetically stable phase compared with the ten-fold coordinated $I4/mmm$ structure in the calculated pressure range. The enthalpy difference between AlB₂-type (or Ni₂In-type) and $I4/mmm$ is considerable. That is there is no tendency to transform to a structure where the coordination number of Cr is beyond 10 up to at least 700 GPa.

To investigate the dynamic stability of three new phases predicted here, the $Pnma$, Fe₂P-type and $I4/mmm$ structures at ultra-high pressures, we have performed *ab initio* lattice-dynamics calculations (Fig. 3). The resultant phonon spectra, lacking any imaginary frequencies imply that the $Pnma$ and $I4/mmm$ phases are dynamically stable. But for the Fe₂P-type phase, the phonon softens below zero around the gamma point in the Brillion zone indicating that it is dynamically unstable. Combining $H–P$ relations and phonon spectra, we might modify the high-pressure phase transition sequence of CrO₂ with rutile-type → CaCl₂-type → pyrite-type → $Pnma$ → $I4/mmm$. It is worthwhile to mention that although recent first-principle calculations have shown that the energetically favor-able Fe₂P-type ZrO₂ is dynamically unstable,[44] the high-pressure and high-temperature XRD experiments have successfully synthesized the Fe₂P-type ZrO₂.[43] This may indicates that the Fe₂P-type phase is dynamically unstable at 0 K, and it can be stable at high temperature and quenched to the ambient temperature. Furthermore, the recent high-pressure experiment has found that VO₂ partially undergoes the $Pnma$–Fe₂P transition at ~100 GPa at room temperature without laser heating.[45] Thus, the Fe₂P-type structure can still be a candidate as an intermediate high-pressure phase between the $Pnma$ and $I4/mmm$ phases. It definitely requires further experimental verification.

3.2. Equation of state and elasticity

Fig. 4 displays the compression of volumes of various phases as a function of pressure and previous experimental and theoretical data are plotted for comparison.[24,27] Our results are generally larger than those obtained by experiments and calculated from simulations. It is widely accepted that GGA tends to overestimate the experimental volume whereas LDA underestimates it. In addition to different exchange correlation potentials, the spin-polarization of Cr is introduced in the present study, which can also cause a larger calculated volume of one compound.

The volume reduction through the rutile–CaCl₂ transition is marginal, specifically less than 0.5%, corresponding to the strain-driven distortive phase transition [Fig. 1(a) and (b)].[24] This can also be supported by the calculated average Cr–O bond distance (d_{av}) shown in Fig. 5, where the evolution of Cr–O bond distances is continuous through the rutile–CaCl₂ transition at 12 GPa. (The average bond distance is defined as

$$d_{av} = \frac{\sum\limits_{j} d_j \exp[1 - (d_j/d_{av})^6]}{\sum\limits_{j} \exp[1 - (d_j/d_{av})^6]}.$$[46,47] d_{av} is obtained self-

consistently.). The volume collapse is 5.1% for the CaCl₂–

structural transition is calculated to occur at 47 GPa whereas Wu *et al.*[27] predicted it to be 23.9 GPa. As shown in Table 1, data from Wu *et al.* are perfectly consistent with our results of the NM pyrite-type CrO₂. However, our calculations demonstrate that the FM pyrite-type CrO₂ is more stable than the NM phase up to at least 200 GPa (Fig. 2). This may explain the difference mentioned above. The previous study predicted an intermediate PbO₂-type phase between the CaCl₂-type and pyrite-type CrO₂.[28] Though Fig. 2 presents that the enthalpy difference between the PbO₂-type and pyrite-type CrO₂ is marginal, our results imply a direct transition from CaCl₂-type to pyrite-type. This can be also supported by the previous high-pressure XRD experiment, which has revealed that the CaCl₂-type CrO₂ is stable up to about 50 GPa.[24] In addition, previous studies simply considered the CaF₂-type structure as the high-pressure post-pyrite phase of CrO₂ neglecting other structures.[25] The present simulation demonstrates that neither the FM CaF₂-type nor the NM CaF₂-type is a stable high-pressure phase. Instead, the $Pnma$ structure becomes energetically favorable compared with the pyrite-type structure above 124 GPa. We further predict that at ultra-high pressures the Fe₂P-type and $I4/mmm$ structures are energetically stable for CrO₂, both of which have been also identified as

Table 2 Calculated lattice parameters and atomic coordinates of rutile-type, $CaCl_2$-type, pyrite-type, *Pnma*, Fe_2P-type and *I4/mmm* CrO_2 under different conditions. The previous experimental and theoretical data are given for comparison

| Phase | Pressure (GPa) | *a* (Å) | *b* (Å) | *c* (Å) | Site | Wyckoff symbol | Internal coordinates | | | Method and reference |
							x	*y*	*z*	
Rutile (*P4₂/mnm*)	0	4.459	4.459	2.929	Cr	2a	0	0	0	This study
					O	4f	0.3037	0.3037	0	
Rutile	0	4.421	4.421	2.916	Cr	2a	0	0	0	Exp.[24]
					O	4f	0.301	0.301	0	
Rutile	0	4.456	4.456	2.829	Cr	2a	0	0	0	LDA[27]
					O	4f	0.2999	0.2999	0	
$CaCl_2$ (*Pnnm*)	12	4.409	4.334	2.893	Cr	2a	0	0	0	This study
					O	4g	0.3105	0.2945	0	
$CaCl_2$	14	4.387	4.282	2.878	Cr	2a	0	0	0	Exp.[24]
					O	4g	0.299	0.272	0	
$CaCl_2$	14	4.393	4.291	2.881	Cr	2a	0	0	0	GGA[28]
					O	4g	0.312	0.291	0	
Pyrite (*Pa3̄*)	47	4.538	4.538	4.538	Cr	4a	0	0	0	This study
					O	8c	0.3533	0.3533	0.3533	
Pyrite	46	4.524	4.524	4.524	Cr	4a	0	0	0	GGA[28]
					O	8c	0.353	0.353	0.353	
Pnma	128	4.876	2.541	6.066	Cr	4c	0.2551	1/4	0.9049	This study
					O1	4c	0.3676	1/4	0.5979	
					O2	4c	0.4815	1/4	0.1494	
Fe_2P (*P6̄2m*)	286	4.866	4.866	2.308	Cr1	1b	0	0	0.5	This study
					Cr2	2c	1/3	2/3	0	
					O1	3f	0.2698	0	0	
					O2	3g	0.6045	0	0.5	
I4/mmm	463	2.220	2.220	5.605	Cr	2b	0.5	0.5	0	This study
					O	4e	0	0	0.1603	

pyrite transition, and 7.7% for the pyrite–*Pnma* transition (Fig. 4). It indicates that two transitions are both first-order. Fig. 5 and Table 2 demonstrate that the large volume collapse at the $CaCl_2$–pyrite transition is due to the reconstruction of ions but not to the compression of the nearest-neighbor Cr–O distances [Fig. 1(b) and (c)]. The compression of Cr–O distances
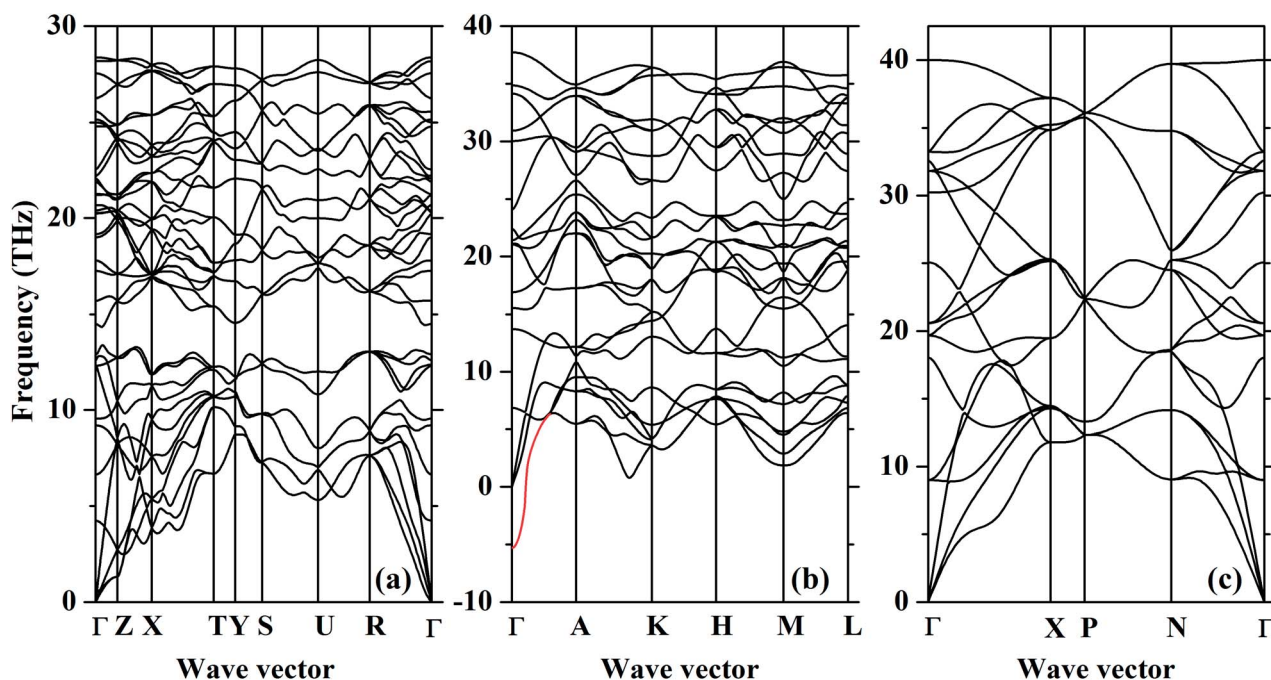

Fig. 3 The phonon dispersions of the (a) *Pnma*, (b) Fe_2P-type and (c) *I4/mmm* CrO_2 at 128 GPa, 386 GPa and 463 GPa, respectively. The red line indicates the phonon softening.
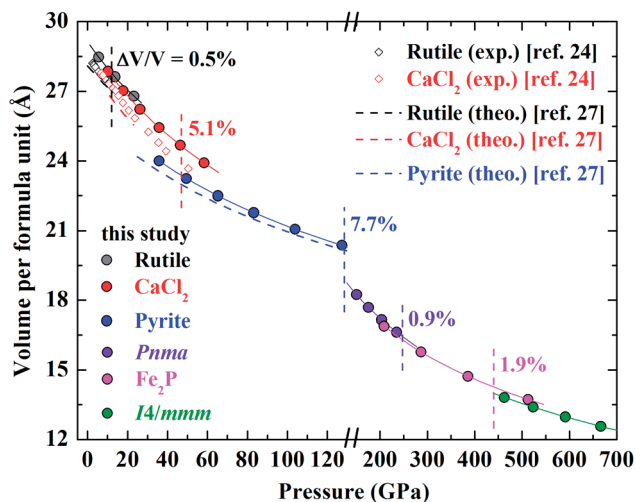
Fig. 4 Calculated volume per formula unit of the rutile-type, $CaCl_2$-type, pyrite-type, *Pnma*, Fe_2P-type and *I4/mmm* CrO_2 as a function of pressure. The solid lines are fitted by the third-order Birch–Murnaghan equation of state. The volume collapse through the structural transition is marked. The previous experimental (black and red open diamonds[24]) and theoretical (black, red and blue dashed lines[27]) data are plotted for comparison.

at high pressures leads to the abrupt volume change at the pyrite–*Pnma* transition [Fig. 1(d), 4 and 5]. The effective coordination number (ECoN) of Cr in the *Pnma* phase increases rapidly from 7.24 at ~128 GPa to 7.73 at ~235 GPa. (The effective coordination number is defined as $ECoN = \sum_j \exp[1 - (d_j/d_{av})^6]$[46,47]). ECoN of Cr in the Fe_2P-type phase is 8.3–8.5 closer to the ideal value 9. Thus, d_{av} decreases through the *Pnma*–Fe_2P transition. The volume variation from *Pnma* to Fe_2P-type and further to *I4/mmm* is 0.9% at 247 GPa and 1.9% at 440 GPa, respectively. It is comparable to that of structural transitions in similar compounds.[17,19,41–43] Though the volume reduction is typically smaller than the aforementioned ones, it may have important contributions to stabilize the high-pressure polymorphs of CrO_2. As displayed in Fig. 5, both the dense polyhedral packing and the compression of the nearest-neighbor Cr–O bond distances contribute to the volume variation [Fig. 1(e) and (f)].

As for the zero-pressure bulk modulus K_0 of different polymorphs of CrO_2, none of them are less than 200 GPa (Table 1). K_0 of CrO_2 generally increases after transforming into a new high-pressure phase except K_0 of the $CaCl_2$-type CrO_2. The distortion of the $CaCl_2$-type structure upon compression mainly accounts for such a reduction. It is worthwhile to note that K_0 of the ten-fold coordinated *I4/mmm* CrO_2 exceeds 300 GPa, which might be a potential super-hard material or could be utilized to explore novel super-hard materials.

3.3. Magnetic and electronic properties

As reported by previous studies, the rutile-type CrO_2 is FM at ambient conditions.[23] CrO_2 keeps FM through the rutile–$CaCl_2$–pyrite transition upon compression up to about 120 GPa (Fig. 6).
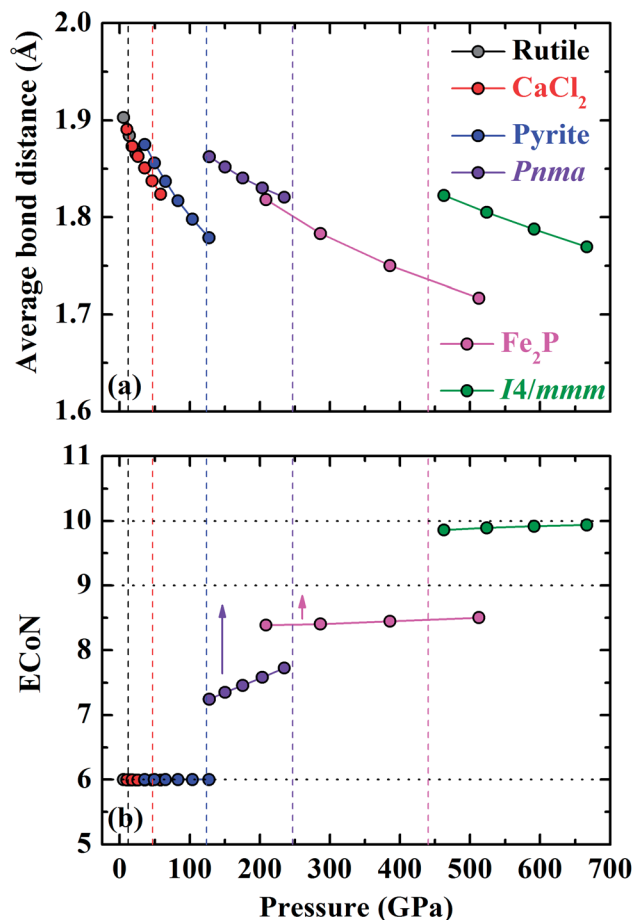

Fig. 5 Calculated (a) average Cr–O bond distance and (b) effective coordination number (ECoN) of different CrO_2 phases as a function of pressure. The vertical dashed lines represent phase transitions. The horizontal dotted lines represent ideal coordination numbers for different structures.

The variation of the magnetic moment per Cr is continuous through the rutile–$CaCl_2$ transition and there is slight increase of the magnetic moment by 0.08 μB at the $CaCl_2$–pyrite transition. As shown in Fig. 6, the pressure slightly affects the magnetic moment of Cr of the FM state. Specifically, the slopes of magnetic moment reductions *versus* pressure are −0.0028 for rutile-type, −0.0008 for $CaCl_2$-type and −0.0014 for pyrite-type, respectively. A magnetic collapse where the sub-lattice magnetic moment per Cr drops from ~1.95 μB to 0 μB is observed at the transition from pyrite-type to *Pnma* at 124 GPa indicating an FM–NM transition (Fig. 6). CrO_2 keeps NM up to 700 GPa considered in the present study. Our results do not support the FM–NM–FM transition proposed by Kim *et al.*[26] Comparing previous investigations with our data, we are able to find out that magnetism affects not only the structural stability of CrO_2 at high pressures but also other physical properties such as elasticity.[26–28]

The DOS of various energetically favorable CrO_2 phases at high pressures calculated by the GGA + *U* method are plotted in Fig. 7. In the rutile-type structure at ambient pressure [Fig. 7(a) and 8], the total DOS in the spin-up state crosses the Fermi level
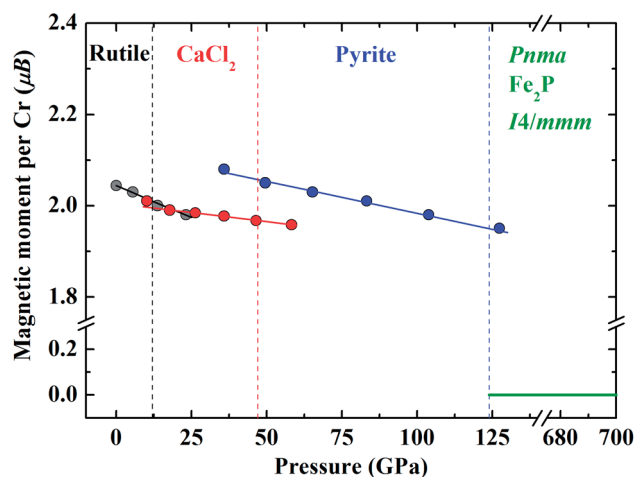
Fig. 6 Calculated sub-lattice magnetic moment per Cr in different CrO$_2$ phases as a function of pressure.

exhibiting metallic whereas there is a gap of 2.07 eV in the spin-down state indicating the semiconducting property. These confirm the HM character of the rutile-type CrO$_2$ at ambient pressure. Upon compression, CrO$_2$ keeps its half-metallicity at the transition to CaCl$_2$-type, even further to pyrite-type (Fig. 7b and c). There is no discontinuity in the variation of the gap in the spin-down state across the rutile–CaCl$_2$ transition (Fig. 8). The gap of the CaCl$_2$-type CrO$_2$ drops ∼0.2 eV at ∼35 GPa. It may be related to the softening of the B$_{1g}$ phonon mode as observed

in the high-pressure Raman experiment.[24] The gap in the spin-down state of the pyrite-type CrO$_2$ reduces gradually upon compression implying the decrease of its half-metallicity at high pressures. At the transition to the *Pnma* structure, CrO$_2$ becomes metallic demonstrating that its half-metallicity is destroyed by pressure [Fig. 7(d) and 8]. The Fe$_2$P-type and *I4/mmm* CrO$_2$ still exhibit metallic at least in the calculated pressure range [Fig. 7(e) and (f) and 8]. The contribution of 2p electrons of O to the conducting band is more pronounced in the Fe$_2$P-type or *I4/mmm* structure than that in the *Pnma* structure. Compared with the first three structures (rutile-type, CaCl$_2$-type and pyrite-type), the 3d electrons of Cr and 2p electrons of O both become more delocalized within the last three structures (*Pnma*, Fe$_2$P-type and *I4/mmm*) resulting in an enhancement of the hybridization between 3d electrons of Cr and 2p electrons of O. As mentioned above, an FM–NM transition with the magnetic collapse of Cr is observed at the pyrite–*Pnma* transition. In combination with the analysis of DOS of various CrO$_2$ phases, we may propose that with increasing pressure an FM–NM transition accompanied by a magnetic collapse delocalizes the 3d electrons of Cr leading to the metallic character of CrO$_2$.

3.4. Comparison with other AO$_2$ compounds

Extensive experimental and theoretical simulations have been performed on AO$_2$ compounds to investigate their stable high-pressure polymorphs. For the fourth main-group element
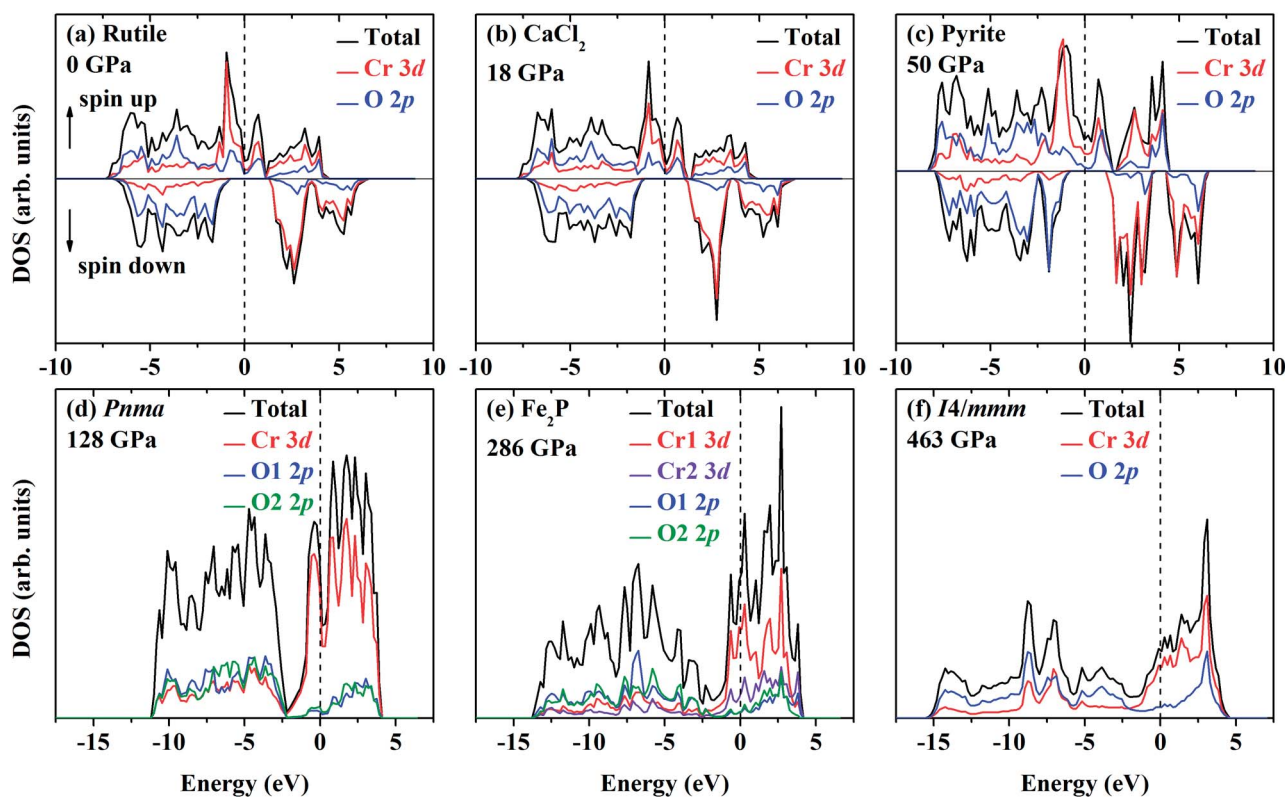

Fig. 7 Calculated DOS of various CrO$_2$ phases under different conditions by the GGA + U method. The total DOS, partial DOS of Cr and O at each equivalent atomic site are marked. The Fermi level is indicated by the vertical dashed line. (a) Rutile-type at 0 GPa, (b) CaCl$_2$-type at 18 GPa, (c) pyrite-type at 50 GPa, (d) *Pnma* at 128 GPa, (e) Fe$_2$P-type at 286 GPa and (f) *I4/mmm* at 463 GPa.
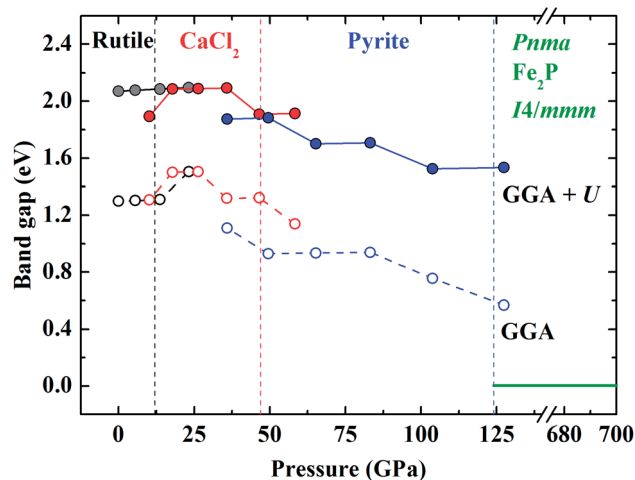
Fig. 8   Calculated band gaps in the spin-down state of various CrO_2 phases as a function of pressure by the GGA and GGA + U methods.

dioxides except CO_2, they can undergo a transition to the *Pnma* structure at relevant high-pressure conditions.[42,48–51] SiO_2 and GeO_2 are predicted to undergo the *Pnma*–Fe_2P transition upon further compression.[17,18,42] The *Pnma*–Fe_2P transition of TiO_2 is predicted to occur at 161 GPa by the GGA method and confirmed by *in situ* XRD at 200 GPa and 3000 K.[41] Experimental and theoretical studies have also verified similar transitions in ZrO_2.[43] According to these available data and our results, we have plotted the transition pressure to the *Pnma* or Fe_2P-type structure (noted by P_P or P_F) for AO_2 compounds *versus* the ionic radius of cations (noted by I_r) (Fig. 9). The ionic radius is the value of the six-fold coordinated cation with the chemical valence of +4.[52] These dioxides can be divided into two groups: main-group element dioxides with unoccupied d orbitals and transition metal dioxides. As shown in Fig. 9, P_P or P_F for transition metal dioxides is much lower than that for main-group element dioxides. For main-group element dioxides, P_P decreases significantly with I_r compared with P_F [Fig. 9(a)]. For transition metal dioxides, P_P or P_F can be roughly considered to reduce linearly with I_r [Fig. 9(b)]. Either theoretical or experimental P_F of VO_2 is much lower than that of TiO_2 or CrO_2. At room temperature, VO_2 crystallizes in the monoclinic $P2_1/c$ structure, a distorted rutile-type form. The distortion significantly affects the structural characteristics and physical properties of VO_2 upon compression. The quasi-hydrostatic or non-hydrostatic condition in high-pressure diamond anvil cell experiments may contribute to or even promote the transition to the Fe_2P-type structure.[45] P_P and P_F of CrO_2 are a little larger. It may be related to the fact that CrO_2 have unpaired 3d electrons. The existence of magnetism in CrO_2 may stabilize the pyrite-type phase, postponing the transition to the *Pnma* phase. Xie *et al.*[45] also take the high-pressure structural evolution of RuO_2 as an example to illustrate the phase transition route of $CaCl_2$–pyrite–CaF_2. The difference of oxygen coordination between VO_2 and RuO_2 leads to different evolution patterns. In the present study, the FM CaF_2-type CrO_2 is much more stable than the NM phase (Fig. 2). But the NM *Pnma* CrO_2 is

energetically favorable compared with aforementioned two phases. The magnetic collapse of Cr can make contributions to favor the pyrite–*Pnma* transition rather than the pyrite–CaF_2 transition. The available data for the pressure-induced phase transition to the $I4/mmm$ structure are too limited and there is no significant relation between the transition pressure to the $I4/mmm$ structure and I_r. In terms of FeO_2 in the recent study, we have predicted a transition sequence of pyrite–$R\bar{3}m$–$I4/mmm$ at high pressures, different from present calculated results.[53] And the stable region of the $R\bar{3}m$ FeO_2 has a span of ~1200 GPa whereas the $R\bar{3}m$ CrO_2 is energetically unfavorable in the present calculated pressure range. Therefore, this can serve as an indirect evidence that the chemical valence of iron cation is not +4 in FeO_2 under ultra-high pressure.

The EoS of the *Pnma* TiO_2 and ZrO_2 have been also obtained by means of high-pressure XRD experiments.[54,55] These results show that K_0 of either TiO_2 or ZrO_2 is larger than 400 GPa. However, recent first-principle calculations or updated XRD data demonstrate that they are both smaller than 300 GPa, *i.e.* 250–290 GPa for TiO_2 and ~286 GPa for ZrO_2.[12,41,43] It is thus worthwhile to mention that K_0 of the *Pnma* phase slightly
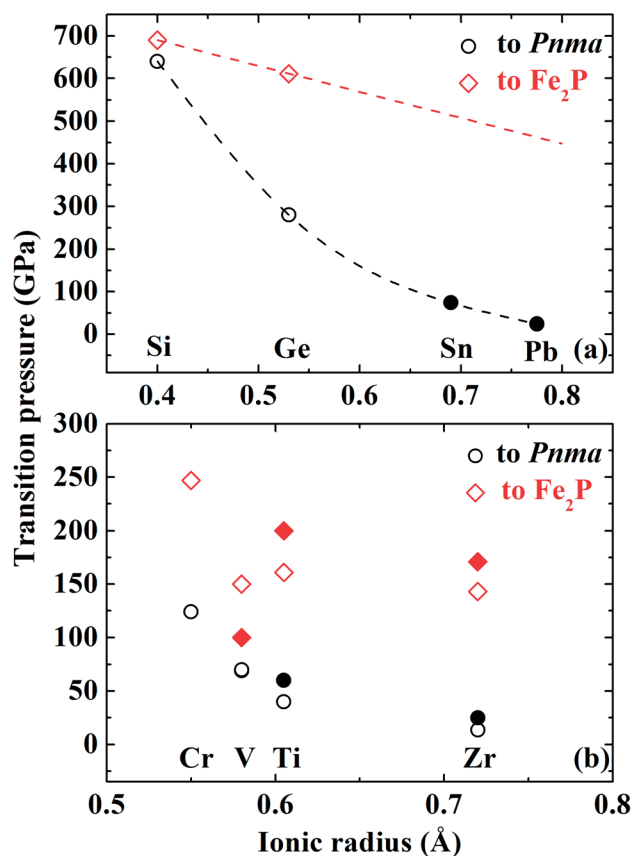

Fig. 9   Correlation plot between the transition pressure to the *Pnma* or Fe_2P-type structure for AO_2 compounds and the ionic radius of cations. The ionic radius of the horizontal ordinate is the value of the six-fold coordinated cation with the chemical valence of +4.[51] The circle and diamond marks represent the transition pressure to *Pnma* and Fe_2P-type, respectively. The open and solid marks represent results obtained by simulations and experiments, respectively.[17,41–43,45,50,51]

increases with I_r. As displayed in Fig. 5(b), ECoN of Cr in the *Pnma* phase is much smaller than nine. It increases rapidly upon compression, indicating the rapid compression of the longest Cr–O bond as a function of pressure. This may result in a smaller K_0. Whereas those with high ECoN may have a larger K_0.

As for the electronic property, the HM CrO_2 is predicted to become metallic through the pyrite–*Pnma* structural transition and keep its metallicity up to 700 GPa. Lyle et al.[19] have predicted the closure of the band gap in TiO_2 and SiO_2 through the Fe_2P–$I4/mmm$ transition at 650 GPa and 9800 GPa, respectively. While FeO_2 is metallic even in the deep lower mantle conditions.[10,56] These thus lead to the conclusion that many of the $I4/mmm$ AO_2 compounds can exhibit metallic, to some extent, independent of their chemical valence and ionic radii of cations. That is the structural character of $I4/mmm$ itself strongly affects the electronic property of AO_2 compounds with the $I4/mmm$ structure upon compression. This can provide an alternative method to explore and synthesize metallic AO_2 materials at high pressures.

4. Conclusions

In conclusion, the high-pressure behavior of CrO_2 has been studied based on first-principle density functional theory. CrO_2 is predicted to undergo a structural transition sequence of rutile-type → $CaCl_2$-type → pyrite-type → *Pnma* → (Fe_2P-type→) $I4/mmm$ at high pressures. Through the pyrite–*Pnma* transition, a magnetic collapse in CrO_2 where the magnetic moment drops from ~2 μB to 0 μB is observed accompanied by a half-metal to metal crossover. The equation of state for different phases of CrO_2 are determined and the elasticity of CrO_2 at high pressures is also discussed in detail. Finally, we summarize the high-pressure behavior of various AO_2 compounds, such as the phase transition pressure, elastic and electronic properties.

Conflicts of interest

There are no conflicts to declare.

Acknowledgements

References

1 A. Fujishima and H. Kenichi, *Nature*, 1972, **238**, 37–38.

2 B. O'Regan and M. Grätzel, *Nature*, 1991, **353**, 737–740.

3 U. Bach, D. Lupo, P. Comte, J. E. Moser, F. Weissörtel, J. Salbeck, H. Spreitzer and M. Grätzel, *Nature*, 1998, **395**, 583–585.

4 M. Nakano, K. Shibuya, D. Okuyama, T. Hatano, S. Ono, M. Kawasaki, Y. Iwasa and Y. Tokura, *Nature*, 2012, **487**, 459–462.

5 N. Shukla, A. V. Thathachary, A. Agrawal, H. Paik, A. Aziz, D. G. Schlom, S. K. Gupta, R. Engel-Herbert and S. Datta, *Nat. Commun.*, 2015, **6**, 7812.

6 H. Yoon, M. Choi, T. Lim, H. Kwon, K. Ihm, J. K. Kim, S. Choi and J. Son, *Nat. Mater.*, 2016, **15**, 1113–1119.

7 S. Lee, K. Hippalgaonkar, F. Yang, J. Hong, C. Ko, J. Suh, K. Liu, K. Wang, J. J. Urban, X. Zhang, C. Dames, S. A. Hartnoll, O. Delaire and J. Wu, *Science*, 2017, **355**, 371–374.

8 R. S. Keizer, S. T. B. Goennenwein, T. M. Klapwijk, G. Miao, G. Xiao and A. Gupta, *Nature*, 2006, **439**, 825–827.

9 Q. Hu, D. Y. Kim, W. Yang, L. Yang, Y. Meng, L. Zhang and H. K. Mao, *Nature*, 2016, **534**, 241–244.

10 S. Huang, S. Qin and X. Wu, *J. Earth Sci.*, 2018, DOI: 10.1007/s12583-018-0836-y.

11 X. Wu, E. Holbig and G. Steinle-Neumann, *J. Phys.: Condens. Matter*, 2010, **22**, 295501.

12 V. Swamy and N. C. Wilson, *J. Phys. Chem. C*, 2014, **118**, 8617–8625.

13 T. Zhu and S. Gao, *J. Phys. Chem. C*, 2014, **118**, 11385–11396.

14 M. Mattesini, J. S. de Almeida, L. Dubrovinsky, N. Dubrovinskaia, B. Johansson and R. Ahuja, *Phys. Rev. B: Condens. Matter Mater. Phys.*, 2004, **70**, 212101.

15 L. Bai, Q. Li, S. A. Corr, Y. Meng, C. Park, S. V. Sinogeikin, C. Ko, J. Wu and G. Shen, *Phys. Rev. B: Condens. Matter Mater. Phys.*, 2015, **91**, 104110.

16 V. Balédent, T. T. F. Cerqueira, R. Sarmiento-Pérez, A. Shukla, C. Bellin, M. Marsi, J. Itié, M. Gatti, M. A. L. Marques, S. Botti and J. Rueff, *Phys. Rev. B*, 2018, **97**, 024107.

17 T. Tsuchiya and J. Tsuchiya, *Proc. Natl. Acad. Sci. U. S. A.*, 2011, **108**, 1252–1255.

18 S. Wu, K. Umemoto, M. Ji, C. Wang, K. Ho and R. M. Wentzcovitch, *Phys. Rev. B: Condens. Matter Mater. Phys.*, 2011, **83**, 184102.

19 M. J. Lyle, C. J. Pickard and R. J. Needs, *Proc. Natl. Acad. Sci. U. S. A.*, 2015, **112**, 6898–6901.

20 H. Niu, A. R. Oganov, X. Chen and D. Li, *Sci. Rep.*, 2015, **5**, 18347.

21 R. J. Soulen Jr, J. M. Byers, M. S. Osofsky, B. Nadgorny, T. Ambrose, S. F. Cheng, P. R. Broussard, C. T. Tanaka, J. Nowak, J. S. Moodera, A. Barry and J. M. D. Coey, *Science*, 1998, **282**, 85–88.

22 R. Yamamoto, Y. Moritomo and A. Nakamura, *Phys. Rev. B: Condens. Matter Mater. Phys.*, 2000, **61**, R5062.

23 K. Schwarz, *J. Phys. F: Met. Phys.*, 1986, **16**, L211.

24 B. R. Maddox, C. S. Yoo, D. Kasinathan, W. E. Pickett and R. T. Scalettar, *Phys. Rev. B: Condens. Matter Mater. Phys.*, 2006, **73**, 144111.

25 V. Srivastava, M. Rajagopalan and S. P. Sanyal, *Eur. Phys. J. B*, 2008, **61**, 131–139.

26 S. Kim, K. Kim, C. Kang and B. I. Min, *Phys. Rev. B*, 2012, **85**, 094106.

27 H. Y. Wu, Y. H. Chen, C. R. Deng and X. F. Su, *Phase Transform.*, 2012, **85**, 708–717.

28 Y. Li and J. Hao, *Solid State Commun.*, 2012, **152**, 1216–1220.

29 A. Yu. Kuznetsov, J. S. de Almeida, L. Dubrovinsky, R. Ahuja, S. K. Kwon, I. Kantor, A. Kantor and N. Guignot, *J. Appl. Phys.*, 2006, **99**, 053909.

30 P. E. Blöchl, *Phys. Rev. B: Condens. Matter Mater. Phys.*, 1994, **50**, 17953–17979.

31 G. Kresse and J. Furthmüller, *Phys. Rev. B: Condens. Matter Mater. Phys.*, 1996, **54**, 11169–11186.

32 G. Kresse and D. Joubert, *Phys. Rev. B: Condens. Matter Mater. Phys.*, 1999, **59**, 1758–1775.

33 J. P. Perdew, K. Burke and M. Ernzerhof, *Phys. Rev. Lett.*, 1996, **77**, 3865–3868.

34 M. A. Korotin, V. I. Anisimov, D. I. Khomskii and G. A. Sawatzky, *Phys. Rev. Lett.*, 1998, **80**, 4305.

35 A. Toropova, G. Kotliar, S. Y. Savrasov and V. S. Oudovenko, *Phys. Rev. B: Condens. Matter Mater. Phys.*, 2015, **71**, 172403.

36 S. L. Dudarev, G. A. Botton, S. Y. Savrasov, C. J. Humphreys and A. P. Sutton, *Phys. Rev. B: Condens. Matter Mater. Phys.*, 1998, **57**, 1505–1509.

37 O. Mustonen, S. Vasala, T. Chou, J. Chen and M. Karppinen, *Phys. Rev. B*, 2016, **93**, 014405.

38 F. D. Murnaghan, *Proc. Natl. Acad. Sci. U. S. A.*, 1994, **30**, 244–247.

39 F. Birch, *Phys. Rev.*, 1947, **71**, 809–824.

40 A. Togo, F. Oba and I. Tanaka, *Phys. Rev. B: Condens. Matter Mater. Phys.*, 2008, **78**, 1–9.

41 H. Dekura, T. Tsuchiya, Y. Kuwayama and J. Tsuchiya, *Phys. Rev. Lett.*, 2011, **107**, 045701.

42 H. Dekura, T. Tsuchiya and J. Tsuchiya, *Phys. Rev. B: Condens. Matter Mater. Phys.*, 2011, **83**, 134114.

43 D. Nishio-Hamane, H. Dekura, Y. Seto and T. Yagi, *Phys. Chem. Miner.*, 2015, **42**, 385–392.

44 J. Zhang, A. R. Oganov, X. Li, M. M. D. Esfahani and H. Dong, *J. Appl. Phys.*, 2017, **121**, 155104.

45 S. Xie, L. Wang, F. Liu, X. Li, L. Bai, V. B. Prakapenka, Z. Cai, H. K. Mao, S. Zhang and H. Liu, *J. Phys. Chem. Lett.*, 2018, **9**, 2388–2393.

46 R. Hoppe, *Z. Kristallogr.*, 1979, **150**, 23–52.

47 J. L. F. Da Silva, *J. Appl. Phys.*, 2011, **109**, 023502.

48 A. R. Oganov, M. J. Gillan and G. D. Price, *Phys. Rev. B: Condens. Matter Mater. Phys.*, 2005, **71**, 064104.

49 K. Umemoto, R. M. Wentzcovitch and P. B. Allen, *Science*, 2006, **311**, 983–986.

50 S. R. Shieh, A. Kubo, T. S. Duffy, V. B. Prakapenka and G. Shen, *Phys. Rev. B: Condens. Matter Mater. Phys.*, 2006, **73**, 014105.

51 B. Grocholski, S. Shim, E. Cottrell and V. B. Prakapenka, *Am. Mineral.*, 2014, **99**, 170–177.

52 R. D. Shannon, *Acta Crystallogr., Sect. A: Cryst. Phys., Diffr., Theor. Gen. Crystallogr.*, 1976, **32**, 751–767.

53 S. Huang, X. Wu and S. Qin, *J. Geophys. Res., [Solid Earth Planets]*, 2018, **123**, 277–284.

54 S. Desgreniers and K. Lagarec, *Phys. Rev. B: Condens. Matter Mater. Phys.*, 1999, **59**, 8467–8472.

55 L. S. Dubrovinsky, N. A. Dubrovinskaia, V. Swamy, J. Muscat, N. M. Harrison, R. Ahuja, B. Holm and B. Johansson, *Nature*, 2001, **410**, 653–654.

56 B. G. Jang, D. Y. Kim and J. H. Shim, *Phys. Rev. B*, 2017, **95**, 075144.